Remote Sensing of Environment 215 (2018) 170–183

Contents lists available at ScienceDirect

Remote Sensing of Environment

journal homepage: www.elsevier.com/locate/rse

Mapping canopy defoliation by herbivorous insects at the individual tree level using bi-temporal airborne imaging spectroscopy and LiDAR measurements

Ran Meng[a,*], Philip E. Dennison[b], Feng Zhao[c], Iurii Shendryk[d], Amanda Rickert[a], Ryan P. Hanavan[e], Bruce D. Cook[f], Shawn P. Serbin[a]

[a] Environmental & Climate Sciences Department, Brookhaven National Laboratory, Upton, New York, NY 11973, USA
[b] Department of Geography, University of Utah, Salt Lake City, UT 84112, USA
[c] Department of Geographical Sciences, University of Maryland, 1165 Lefrak Hall, College Park, MD 20742, USA
[d] CSIRO, Agriculture and Food, St. Lucia, Brisbane, QLD 4067, Australia
[e] USDA Forest Service, Northeastern Area State & Private Forestry, 271 Mast Rd., Durham, NH 03824, USA
[f] Biospheric Sciences Branch, NASA Goddard Space Flight Center, Greenbelt, MD 20742, USA

ARTICLE INFO

Keywords:
Forest infestation
MESMA
Invasive species
LiDAR
Hyperspectral
Data fusion

ABSTRACT

Defoliation by herbivorous insects is a widespread forest disturbance driver, affecting global forest health and ecosystem dynamics. Compared with time- and labor-intensive field surveys, remote sensing provides the only realistic approach to mapping canopy defoliation by herbivorous insects over large spatial and temporal scales. However, the spectral and structural signatures of defoliation by insects at the individual tree level have not been well studied. Additionally, the predictive power of spectral and structural metrics for mapping canopy defoliation has seldom been compared. These critical knowledge gaps prevent us from consistently detecting and mapping canopy defoliation by herbivorous insects across multiple scales. During the peak of a gypsy moth outbreak in Long Island, New York in summer 2016, we leveraged bi-temporal airborne imaging spectroscopy (IS, i.e., hyperspectral imaging) and LiDAR measurements at 1 m spatial resolution to explore the spectral and structural signatures of canopy defoliation in a mixed oak-pine forest. We determined that red edge and near-infrared spectral regions within the IS data were most sensitive to crown-scale defoliation severity. LiDAR measurements including B70 (i.e., 70th bincentile height), intensity skewness, and kurtosis were effectively able to detect structural changes caused by herbivorous insects. In addition to canopy leaf loss, increased exposure of understory and non-photosynthetic materials contributed to the detected spectral and structural signatures. Comparing the ability of individual sensors to map canopy defoliation, the LiDAR-only Ordinary Least-Square (OLS) model performed better than the IS-only model (Adj. R-squared = 0.77, RMSE = 15.37% vs. Adj. R-squared = 0.63, RMSE = 19.11%). The IS + LiDAR model improved on performance of the individual sensors (Adj. R-squared = 0.81, RMSE = 14.46%). Our study improves our understanding of spectral and structural signatures of defoliation by herbivorous insects and presents a novel approach for mapping insect defoliation at the individual tree level. Additionally, with the current and next generation of spaceborne sensors (e.g., WorldView-3, Landsat, Sentinel-2, HyspIRI, and GEDI), higher accuracy and frequent monitoring of insect defoliation may become more feasible across a range of spatial scales, which are critical for ecological research and management of forest resources including the economic consequences of forest insect infestations (e.g., reduced growth and increased mortality), as well as for informing and testing of carbon cycle models.

1. Introduction

Infestation by insects and pathogens is one of most widespread disturbances in forest ecosystems, affecting forest health, ecosystem services, carbon dynamics, and species composition across the globe (Ayres and Lombardero, 2000; Kautz et al., 2017a; Kautz et al., 2017b; Seidl et al., 2017; Senf et al., 2017c). In the United States, forest infestation was estimated to be 20 M ha per year, of which 25–50% was attributable to defoliation by herbivorous insects (Dale et al., 2001; Kautz et al., 2017b). The exotic gypsy moth (*Lymantria dispar L.*) is one

* Corresponding author.
E-mail address: ranmeng@bnl.gov (R. Meng).

https://doi.org/10.1016/j.rse.2018.06.008
Received 22 November 2017; Received in revised form 5 June 2018; Accepted 6 June 2018

of the chief defoliators across the northeastern United States. Gypsy moth larvae (caterpillars) feed on leaves of host trees and can defoliate 0.5–1.0 M ha forest per year on average and > 5.0 M ha in peak years (Elkinton and Liebhold, 1990; Man, 2010). Also, because the range of gypsy moth is still expanding, studying defoliation by gypsy moth is of high research and management interest (De Beurs and Townsend, 2008; Foster et al., 2013; Spruce et al., 2011; Thompson et al., 2017; Townsend et al., 2012).

Insect defoliation does not necessarily result in immediate tree mortality, but can reduce tree growth and trees' resilience to secondary pressures (e.g., drought, wildfire, and hurricanes) (Dale et al., 2001; Gandhi and Herms, 2010; Naidoo and Lechowicz, 2001). Defoliation can also kill trees after successive defoliation events (Dudley and Bean, 2012; Kegg, 1971), leading to significant ecological and economic consequences and carbon dynamics (Clark et al., 2010; Coyle et al., 2008; Kenis et al., 2009). Effective detection and monitoring of insect defoliation has thus long been a central focus in the remote sensing, forest ecology and management communities (Coulson et al., 1999; Foster et al., 2013; Landsber and Ohmart, 1989; Townsend et al., 2012), and becomes a pressing issue with increasing evidence showing positive interactions between forest infestation and drier and warmer climate (Kolb et al., 2016; Logan et al., 2003; Seidl et al., 2014; Seidl et al., 2017).

Remote sensing provides the only realistic way for mapping defoliation by herbivorous insects over large spatial and temporal scales (Rullan-Silva et al., 2013; Senf et al., 2017c; Townsend et al., 2012). A wide range of remote sensing data has demonstrated the capacity to monitor spatial-temporal patterns of defoliation by herbivorous insects, including spaceborne multispectral data (e.g., 2 m WorldView-2, 10 m SPOT, 30 m Landsat, and 250 m MODIS) (De Beurs and Townsend, 2008; Dennison et al., 2009; Franklin et al., 2008; Ji et al., 2017; Meng et al., 2012; Nagler et al., 2014; Oumar and Mutanga, 2014; Spruce et al., 2011; Townsend et al., 2012), airborne imaging spectroscopy (IS, i.e., hyperspectral imaging) data (e.g., 5 m HyMap and18 m AVIRIS) (Fassnacht et al., 2014; Hanavan et al., 2015; Somers et al., 2010), and airborne Light Detection and Ranging (LiDAR) data (Hanssen and Solberg, 2007; Solberg et al., 2006) at multiple spatial scales. Numerous remote sensing-based approaches to mapping defoliation by herbivorous insects have also been developed and applied, such as vegetation indices (Spruce et al., 2011; Townsend et al., 2012), spectral mixture analysis (Radeloff et al., 1999; Somers et al., 2010), and image classification (Kantola et al., 2010; Oumar and Mutanga, 2014; Senf et al., 2015).

Vegetation indices applied to 30 m Landsat data have been used most widely, e.g., (Hurley et al., 2004; Pasquarella et al., 2017; Townsend et al., 2012), however, these approaches focus solely on broadband spectral responses (i.e., red, near-infrared (NIR), and shortwave near-infrared (SWIR)) to canopy defoliation at ≥ 30 m scales. Very high spatial resolution (VHR, ≤ 5 m) multi-spectral sensors, such as GeoEye, QuickBird, and WorldView-2, have been used for mapping and predicting canopy defoliation with relatively higher accuracies, e.g., (Dennison et al., 2010; Oumar and Mutanga, 2014; White et al., 2005; Wulder et al., 2008), but most of these studies mainly focused on mapping advanced stages of canopy defoliation (e.g., tree mortality). More importantly, only a few studies have explored the utility of IS or LiDAR for measuring defoliation severity of deciduous broadleaved trees in temperate forest (Hanavan et al., 2015; Hanssen and Solberg, 2007; Shendryk et al., 2016; Solberg et al., 2006; Somers et al., 2010). Determination of high resolution spectral and structural signatures of canopy defoliation severity of deciduous broadleaved trees in temperate forest is critical for consistent and precise forest health monitoring at global scale (Millar and Stephenson, 2015; Trumbore et al., 2015), but these signatures are still poorly understood. Additionally, few studies have compared the predictive power of spectral and structural metrics and their combination for measuring defoliation severity, and the combined use of spectral and structural metrics has broad implications for the development of next-generation remote sensing frameworks for forest health monitoring (Lausch et al., 2016; White et al., 2016). These critical knowledge gaps need to be filled for consistent and precise detection and mapping of defoliation by herbivorous insects at VHR, which will enable more effective operational forest management (e.g., insect control and fire suppression) and improve our understanding of the effects of insect outbreaks on forest ecology, ecosystem services, and carbon dynamics (Black, 2005; Clark et al., 2010; Kenis et al., 2009; Oumar and Mutanga, 2014).

The development of airborne remote sensing platforms, including VHR optical IS and structual LiDAR instruments, can help resolve these knowledge gaps (Asner et al., 2017; Cook et al., 2013). By measuring continuous narrowband spectral information, IS data can enhance our ability to remotely assess forest health (Hanavan et al., 2015; Somers et al., 2010). By retrieving detailed three-dimensional information about tree canopies with a high density of laser pulses, LiDAR provides new opportunities for monitoring forest health in the context of the detection and mapping of forest infestations (Hanssen and Solberg, 2007; Shendryk et al., 2016; Solberg et al., 2006). Most prior applications of IS or LiDAR to mapping defoliation by herbivorous insects have focused on pine trees and wood-boring beetles (e.g., mountain pine beetles) (Hanssen and Solberg, 2007; Senf et al., 2017c; Solberg et al., 2006), and the potential of combined IS and LiDAR measurements has not been sufficiently assessed and compared for mapping defoliation severity of deciduous broadleaf forests by defoliators like gypsy moth.

Our objective is to explore the crown-scale spectral and structural signatures of canopy defoliation by gypsy moth caterpillars across a defoliation severity gradient and present a novel approach for mapping crown-scale canopy defoliation, which can be easily transferable to other forest ecosystems or forest infestation types. Likely because of consecutive dry springs for the past several years (2014–2016), a severe gypsy moth outbreak occurred and caused widespread canopy defoliation in northeastern United States in early summer 2016 (Pasquarella et al., 2017). During the peak of this defoliation event (i.e., June 14th, 2016), we leveraged the airborne remote sensing platform (i.e., NASA Goddard's LiDAR, Hyperspectral and Thermal (G-LiHT); Cook et al., 2013) to simultaneously measure optical IS and structural LiDAR information at VHR in a mixed oak-pine forest. We chose this study area, because we previously surveyed this area with the airborne G-LiHT platform one year before on an anniversary date (i.e., June 15th, 2015). During ground measurements, we estimated percentage of leaf area remaining, ranging between 0% and 100%, to record defoliation severity at the individual tree level. As defoliation severity is the inverse of percentage of leaf area remaining, 0% leaf area remaining refers to complete canopy defoliation.

Using G-LiHT IS and LiDAR datasets and corresponding ground measurements, we addressed the following research questions: (1) At the crown scale, what are the spectral and structural signatures of defoliation by herbivorous insects across a defoliation severity gradient? (2) Can biophysical effects (i.e., canopy leaf loss and increased non-photosynthetic material and understory exposure) explain the detected spectral and structural signatures of defoliation by herbivorous insects? (3) What are the differences in predictive power of IS and LiDAR for mapping crown-scale defoliation? (4) Can the combined use of IS and LiDAR improve mapping accuracy?

2. Materials

2.1. Study area

We examined a gypsy moth outbreak event in several mixed oak-pine forest stands located in the Long Island Pine Barrens ecoregion, New York (Fig. 1) during the summer of 2016. The study area has undergone several outbreaks of gypsy moth defoliation for the past three decades. The study area has sandy-flat soils and a moderate-humid climate with evenly-distributed annual precipitation

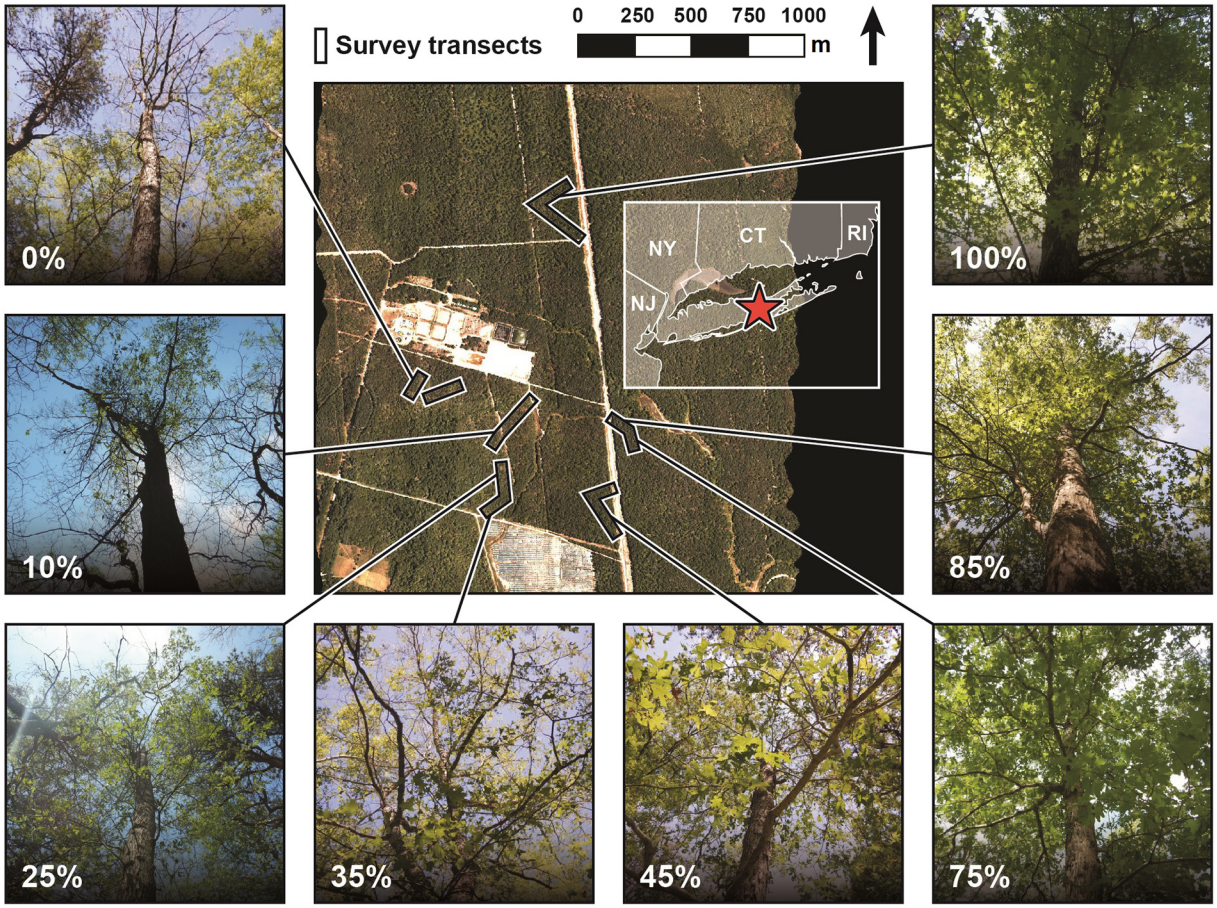

Fig. 1. Crown-scale defoliation survey transects within the study area (the background imagery is the true color RGB composition (657 nm (red), 564 nm (green), and 484 nm (blue)) derived from NASA Goddard's LiDAR, Hyperspectral and Thermal (G-LiHT) measurements acquired on June 14, 2016); in-situ pictures showing crown-scale defoliation severity scores (i.e., percentage of leaf area remaining). (For interpretation of the references to color in this figure legend, the reader is referred to the web version of this article.)

(Kurczewski and Boyle, 2000). Annual precipitation is approximately 1200 mm; annual daily mean temperature is −4.8 °C in January and 21.9 °C in July. Mixed with pitch pine (*Pinus rigida*), the dominant species of broadleaf trees in the study areas are white oak (*Quercus alba L.*), scarlet oak (*Quercus coccinea*), and black oak (*Quercus velutina*). Huckleberry (*Gaylussacia baccata K. Koch*) and blueberry (*Vaccinium spp.*) are the two main shrub species in the study area, which have been found to have an inverse canopy cover relationship with trees (Reiners, 1967).

2.2. Aerial survey and data preprocessing

We conducted two aerial surveys of the study area (collectively, 800 ha; Fig. 1), with the airborne G-LiHT platform before and during the peak of the gypsy moth outbreak in summer 2015 (i.e., June 15th, 2015) and 2016 (i.e., June 14th, 2016). The bi-temporal aerial surveys were conducted on a sunny day within 2-h window of local solar noon at a 50° field of view and 200 m average flight altitude. Compared with a single post-disturbance IS and LiDAR dataset, bi-temporal datasets allow measurement of changes in specific tree crowns. G-LiHT consists of a scanning LiDAR, profiling LiDAR, imaging spectrometer, Global Positioning System and Inertial Navigation System (GPS-INS) and time server, data acquisition computer, and downwelling irradiance spectrometer (Cook et al., 2013). The LiDAR data were collected by an onboard aerial laser scanning (ALS) system (Riegl USA, Orlando, FL, USA) with a mean pulse density of 15–20 laser pulses/m^2. The IS sensor (Headwall Photonics, Fitchburg, MA, USA) collected spectra over the 407–1007 nm spectral region in 114 spectral bands with a ≤5 nm increments (full width half maximum) and a 12-bit radiometric resolution at 1 m spatial resolution (Cook et al., 2013). The data used in this study, including at-sensor corrected reflectance (ACR) and georeferenced IS data and coincident LiDAR data at 1 m spatial resolution, can be downloaded from the G-LiHT website (http://gliht.gsfc.nasa.gov/).

To ensure consistent temporal reflectance response, we performed radiometric inter-calibrations for the bi-temporal ACR IS imagery. Specifically, we manually selected 3560 pixels of invariant spectral features (i.e., impervious surfaces) directly on the bi-temporal G-LiHT IS imagery, then we fitted and applied a linear regression model for each IS spectral band, from 2015 against 2016. Inter-calibrated spectra were compared to in situ spectra collected on the ground for data quality check (see Section 2.3 below).

2.3. Field measurements

Because defoliation by gypsy moth caterpillars is an ephemeral process, we conducted field measurements of canopy defoliation at the individual tree level within five days of the 2016 G-LiHT aerial survey. Since gypsy moth caterpillars mainly feed on deciduous broadleaf trees (Lippitt et al., 2008), we only measured defoliation status of oak trees within the study area including black oak, scarlet oak, and white oak. To capture a wide variation of canopy defoliation severity and avoid spatial autocorrelation effects, we established seven variable-length transects ranging between 120 and 250 m within the study area (Fig. 1). Specifically, we randomly started to sample oak trees from the road edge, and measured every oak tree at least 15 m spatially separated in

each transect until reaching the forest interior (Fig. 1).

In total, 91 oak crowns were measured within the study area (Fig. 1). The percentage of leaf area remaining in each survey crown was visually estimated by two technicians separately with 10% intervals, and the two independent estimations were averaged and used as defoliation severity. At the same time, multiple in-situ photos were taken for each survey crown for verifying defoliation status afterwards (Fig. 1). Species and diameter at breast height (DBH) were also recorded. Additionally, for checking the quality and potential spectral calibration of G-LiHT IS data, we used a Spectral Evolution PSR+ 3500 spectrometer (http://www.spectralevolution.com/) to collect the ground spectra during the 2016 G-LiHT aerial survey. Specifically, we collected spectra of different land covers on the ground (e.g., soil, grass, concrete road, and litter), ranging between 350 and 2500 nm, and each ground sample was measured five times. The center coordinates of all survey tree crowns and field spectra sites were recorded with a handheld decimeter-level differential global positioning system (dGPS, Trimble Geo7x). After post-processing, the average horizontal accuracy of recorded coordinates was 0.20 m.

3. Methods

To map crown-scale oak canopy defoliation, our workflow was composed of the following steps: (1) LiDAR-based crown segmentation (i.e., individual tree delineation), (2) analysis of spectral and structural signatures of survey crowns, (3) Multiple Endmember Spectral Mixture Analysis (MESMA) applied to IS data in 2015 and 2015, (4) training and comparison of defoliation models, and (5) crown-scale canopy defoliation mapping (Fig. 2).

3.1. LiDAR-based crown segmentation

We applied a top-down segmentation algorithm (Li et al., 2012) to segment tree crowns from the G-LiHT LiDAR point cloud, as the dense understory of Long Island Pine Barrens ecoregion forest limits bottom-up algorithms for detecting individual tree trunks (Lu et al., 2014; Shendryk et al., 2016). This top-down segmentation algorithm isolates trees individually and sequentially from the point cloud, from the tallest tree to the shortest. Starting from a treetop, a target tree is identified by including nearby points and excluding points of other trees based on their horizontal spacing. The main input parameters of the used top-down segmentation algorithm are 1) search radius (R), which is used for identifying local maxima, 2) horizontal threshold (d_{t1}), which is used for including points to a target tree at height lower than 15 m, 3) horizontal threshold (d_{t2}), which is used for including points to a target tree at height higher than 15 m, and 4) minimum number of points (n) in a target tree (Li et al., 2012). Based on the 18 forest inventory plot data collected in the same forest area from previous studies (Meng et al., 2017) (see Section 1 in Supplementary materials for more details about the forest inventory data), the following combination of parameters: R of 1.5 m, d_{t1} of 1.5 m; d_{t2} of 3.5 m, and n of 10 points were determined and used to segment tree crowns (see Supplementary materials Section 2 for more details about determining optimal segmentation parameters). The segmentation was performed using Digital Forestry Toolbox (Parkan, 2017). We then used the dGPS-recorded coordinates of individual defoliation survey trees to link corresponding polygons of segmented crowns, and used these crown-scale segmentation polygons as the basis for further analysis.

3.2. Multiple endmember spectral mixture analysis (MESMA)

To calculate IS metrics for defoliation mapping and explore the biophysical effects underpinning the spectral and structural signatures of defoliation by gypsy moth caterpillars, we applied MESMA to the G-LiHT IS imagery in 2015 and 2016. MESMA is an expanded version of Linear Spectral Mixture Analysis (LSMA) (Roberts et al., 1998). LSMA

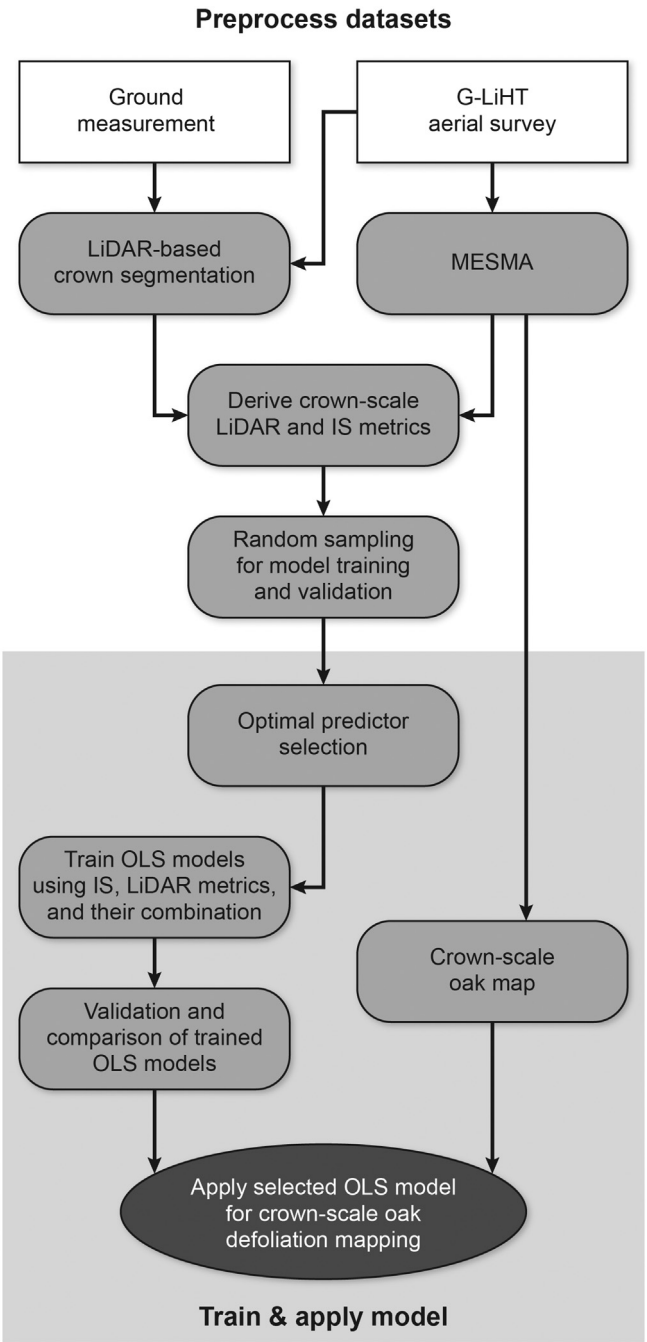

Fig. 2. Workflow in this study for mapping canopy defoliation by herbivorous insects at the individual tree level.

decomposes the reflectance of image mixed pixels using a fixed set of spectrally distinct components (i.e., endmembers), enabling the estimations of the relative contribution of a given cover type (i.e., abundance) to pixel reflectance (Drake et al., 1999). MESMA overcomes the LSMA's constraint of modeling all pixels for a given cover type using the same set of endmembers by allowing the endmember model to vary on a pixel-by-pixel basis (Roberts et al., 1998). Specifically, MESMA can use variable endmembers for different endmember models (e.g., two, three, four or more) to account for within-class spectral variability. Thereby, MESMA can extract biophysical-meaningful information from IS spectra, and has been widely used for remote sensing of forest disturbance studies (Lewis et al., 2017; Meng et al., 2017; Meng et al., 2018; Meng and Zhao, 2017; Quintano et al., 2013).

Our application of MESMA consisted of three key steps: spectral

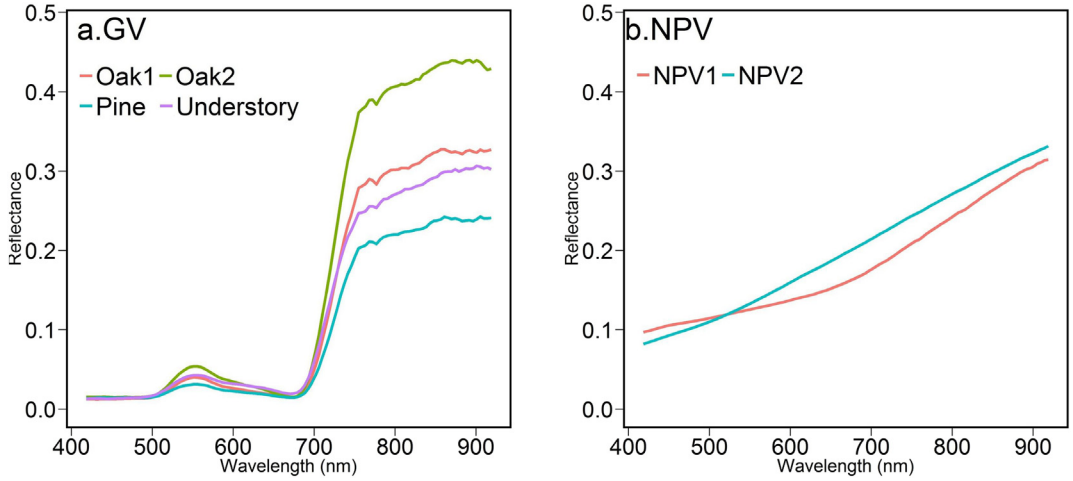

Fig. 3. Green vegetation (GV) (a) and non-photosynthetic vegetation (NPV) (b) endmembers selected for use with MESMA.

library development, selection of optimal endmembers, and modeling. First, we used G-LiHT image spectra to define endmembers for spectral library development. Based on our knowledge of the study area and very high spatial resolution imagery in Google Earth Pro, we manually defined candidate endmembers on the 2016 G-LiHT hyperspectral imagery. Avoiding shadow and edge pixels, we selected about two thousand uniform pixels as candidates for green vegetation (GV) endmembers, including oak, pine, and shrub understory. Endmember Average Root Mean Square Error (EAR; Dennison and Roberts, 2003) was used to select GV endmembers for MESMA. EAR calculates how well each endmember spectrally represents one endmember type. We selected one to two "optimal" endmembers for the following GV types: GV-understory, GV-pine, and GV-oak (Fig. 3a). For non-photosynthetic vegetation (NPV) endmembers, we convolved branch and trunk field spectra collected from the study area (Section 2.3) into G-LiHT spectra (Fig. 3b). Considering the relatively simple cover types in our study area, we assumed that every G-LiHT IS pixel can be modeled by a three endmember model (i.e. GV-NPV-Shadow). We thus applied a three endmember MESMA model to unmix each G-LiHT IS image.

We set the minimum allowable endmember fraction, maximum allowable endmember fraction, and maximum allowable shade fraction to values of 0.05, 1.05 and 1.0, respectively, and the maximum root-mean-square error (RMSE) to 0.025. All constraint values were based on recommendations for the Visualization and Image Processing for Environmental Research (VIPER) Tools software package (Roberts et al., 2007), which was used to implement MESMA. MESMA successfully modeled 91.8% of 2015 IS pixels and 94.5% of 2016 IS pixels.

3.3. LiDAR structural metrics

G-LiHT LiDAR data were used to calculate various structural metrics for mapping defoliation by gypsy moth caterpillars (Table 1). Previous studies have found that LiDAR structural metrics can effectively detect overall structural changes by natural disturbances and thus can be used to assess forest health (Kane et al., 2014; McCarley et al., 2017; Shendryk et al., 2016). We chose these structural metrics, according to their use in other forest disturbance studies (Kane et al., 2014; McCarley et al., 2017; Shendryk et al., 2016). To generate the LiDAR structural metrics, we first binned the bi-temporal G-LiHT LiDAR point clouds into 1-m voxels. Then all LiDAR structural indices were calculated and converted into individual rasters. We calculated all LiDAR-derived structural metrics using LAStools software suite (https://rapidlasso.com/). Not all structural metrics were finally used, and a variable selection process was applied to select optimal predictors for defoliation modeling (Please see Sections 3.4 & 3.5 below).

3.4. Comparison of predictive powers for IS, LiDAR and their combination

To train a robust ordinary least squares (OLS) model for mapping crown-scale canopy defoliation, a preliminary screening was first conducted to select optimal predictors from all available predictors derived from G-LiHT IS and LiDAR data. We first calculated mean, minimum, maximum, and standard deviation values for each individual tree crown polygon described in Section 3.1 for 2015 and 2016 MESMA (i.e., oak, pine, understory, and NPV fraction) and structural metrics (Table 1). Then, based on the survey crown dataset, we fit a linear model and calculated Pearson's correlation coefficient (r) for all combinations of 2016 predictors and percentage of leaf area remaining at the individual tree level. We also evaluated if univariate models between the response variable and each 2016 predictor variable could be better fit with a second-degree polynomial or logistic regression than with a simple linear relationship, but we did not observe evidence for any other than a linear fit. As such to reduce data redundancy, a threshold of an absolute r value of 0.40 was used to exclude predictors with poor predictive power from further analysis. After the predictor screening, the change in remaining predictors (see Fig. 6 below for a complete list) was calculated (Eq. (1)) and used to provide additional predictive variables:

$$Change\ in\ Var = Var_{2015} - Var_{2016} \quad (1)$$

where *Var* is the given variable under study. Then, we performed the following steps for OLS model training and validation: (1) The survey crown dataset was randomly split into training (70%) and validation (30%) dataset. (2) To compare the predictive power of IS, LiDAR, and their combination, the three following options were used for model training: IS: only using IS-derived (i.e., MESMA) variables; LiDAR: only using LiDAR variables; IS + LiDAR: using both IS and LiDAR variables. (3) Using an Akaike Information Criterion (AIC)-based backward method (Burnham and Anderson, 2004), we selected important predictors and trained OLS models for the three options, separately. (4) We applied the three trained OLS models to the validation datasets and assessed their predictive powers using the root mean square error (RMSE; mean Euclidean distance between the prediction in crown-scale oak defoliation and the surveyed oak defoliation) and adjusted R-squared (i.e., the proportion of variability in crown-scale oak defoliation explained by model).

Important variable selection can remove unnecessary predictors and thus reduce collinearity and noise of trained OLS models (Kane et al., 2015; Meng and Dennison, 2015). AIC is a metric commonly used to compare the performances of different OLS models (Yamashita et al., 2007). AIC-based backward method starts all available predictors in the OLS model, and then removes the predictor with lowest AIC

Table 1
Calculated LiDAR-derived structural metrics from 2015 and 2016 G-LiHT aerial data collections used in this study.

Index acronym	LiDAR-derive structural metrics	Interpretation
CHM	Canopy height model	Mean vegetation crown height
COV	Canopy cover	Number of first returns above the cover cutoff (i.e., 5 m) divided by the number of all first returns and output as a percentage
DNS	Canopy density	Number of all points above the cover cutoff (i.e., 5 m) divided by the number of all returns
QAV	Mean quadratic height	Mean of the quadratic height ($\sum_{i=1}^{n} h_i^2/n$), h_i is the height of a return point and n is the number of all points
SKE	Skewness	The skewness of return points
KUR	Kurtosis	The kurtosis of return points
P_{nth}	nth percentile height	nth (i.e., 10, 20, 30, 40, 50, 60, 70, 80, and 90) percentile height value of return points between the ground and the maximum height
Int_ske	Intensity skewness of return intensity	Intensity skewness of return points
Int_kur	Intensity kurtosis of return intensity	Intensity kurtosis of return points
B_{nth}	nth bincentile height	Fraction of return points between the nth (i.e., 10, 20, 30, 40, 50, 60, 70, 80, and 90) percentile height and the maximum height (%)
0–5 m	0–5 m LiDAR return fraction	Fraction of return points within the 0–5 m height interval to the total number of return points (%)
5–10 m	5–10 m LiDAR return fraction	Fraction of return points within the 5–10 m height interval to the total number of return points (%)
10–15 m	10–15 m LiDAR return fraction	Fraction of return points within the 10–15 m height interval to the total number of return points (%)
15–20 m	15–20 m LiDAR return fraction	Fraction of return points within the 15–20 m height interval to the total number of return points (%)
20–35 m	20–35 m LiDAR return fraction	Fraction of all return points within the 20–35 m height interval to the total number of return points (%)

improvement until all predictors in the OLS model contribute significantly to the OLS model (Yamashita et al., 2007). Remaining uncertainties during the current OLS modeling process include the randomness in splitting between training (70%) and validation (30%) datasets and the potential of over-fitting caused by the relative small size dataset (i.e., 91 crowns). Thereby, we repeated the OLS modeling process one hundred times using randomly selected training and validation data, and then summarized the resulting RMSE and adjusted R-squared results to assess the OLS models.

3.5. Mapping crown-scale oak defoliation

To map canopy defoliation by gypsy moth caterpillars at the individual tree level, we trained an OLS IS + LiDAR model using selected important predictors with a frequency of ≥ 60 (showing best performance, see Section 4.4). To avoid over-fitting, we averaged the coefficient values of IS + LiDAR model from the repeat training results (see Table 2 below) for mapping crown-scale oak defoliation across the study area. An oak crown mask was generated based on the 2015 MESMA results: we classified a crown object as oak if > 50% pixels within the crown object polygon had ≥ 0.5 oak endmember fraction value. The accuracy of the oak crown map was assessed using crown-scale oak defoliation and forest inventory field measurements in 2016, and had an overall accuracy of 84% estimated by an error matrix (Table S.1).

The primary assumptions of OLS modeling were also tested and satisfied as below: (1) Normality, by visual analysis of a normal Q-Q plot showing standardized residuals vs. normal scores (Ghasemi and Zahediasl, 2012); (2) Co-linearity, by calculations of variance inflation factors (VIF) with a threshold of 10 (O'brien, 2007); (3) Homoscedasticity, by visual analysis of a plot showing the standardized residuals vs. the standardized predicted values (Griffith, 2009).

Table 2
Selection frequencies of important predictor variables by AIC method during OLS modeling (only predictor variables selected more than once was shown here) and their confidence interval of coefficient values.

Name	Frequency	Option	Chosen or not for final models	95% Confidence interval of coefficient values
Intercept		IS-only		62.06 ± 0.74
Change in NPV fraction	100	IS-only	Yes	318.34 ± 8.61
Oak fraction in 2016	97	IS-only	Yes	35 ± 1.42
Change in understory fraction	95	IS-only	Yes	60.42 ± 1.25
NPV fraction in 2016	86	IS-only	Yes	3058.67 ± 138.86
Change in MESMA oak fraction	9	IS-only	No	N.A.
MESMA understory fraction in 2016	6	IS-only	No	N.A.
Intercept		LiDAR-only		139.36 ± 0.7
B70 in 2016	99	LiDAR-only	Yes	−1.09 ± 0.02
Change in Kurtosis	70	LiDAR-only	Yes	−10.86 ± 0.35
Intensity skewness in 2016	60	LiDAR-only	Yes	−57.95 ± 0.65
Change in intensity skewness	16	LiDAR-only	No	N.A.
B80 in 2016	1	LiDAR-only	No	N.A.
Skewness in 2016	1	LiDAR-only	No	N.A.
Change in skewness	1	LiDAR-only	No	N.A.
Intercept		IS + LiDAR		100.53 ± 0.3
B70 in 2016	98	IS + LiDAR	Yes	−1.12 ± 0.02
MESMA Oak fraction in 2016	97	IS + LiDAR	Yes	36.28 ± 0.8
Change in intensity skewness	69	IS + LiDAR	Yes	20.82 ± 0.57
Change in Kurtosis	38	IS + LiDAR	No	N.A.
Intensity skewness in 2016	13	IS + LiDAR	No	N.A.
Change in B80	8	IS + LiDAR	No	N.A.
MESMA NPV fraction in 2016	2	IS + LiDAR	No	N.A.
Change in MESMA NPV fraction	1	IS + LiDAR	No	N.A.

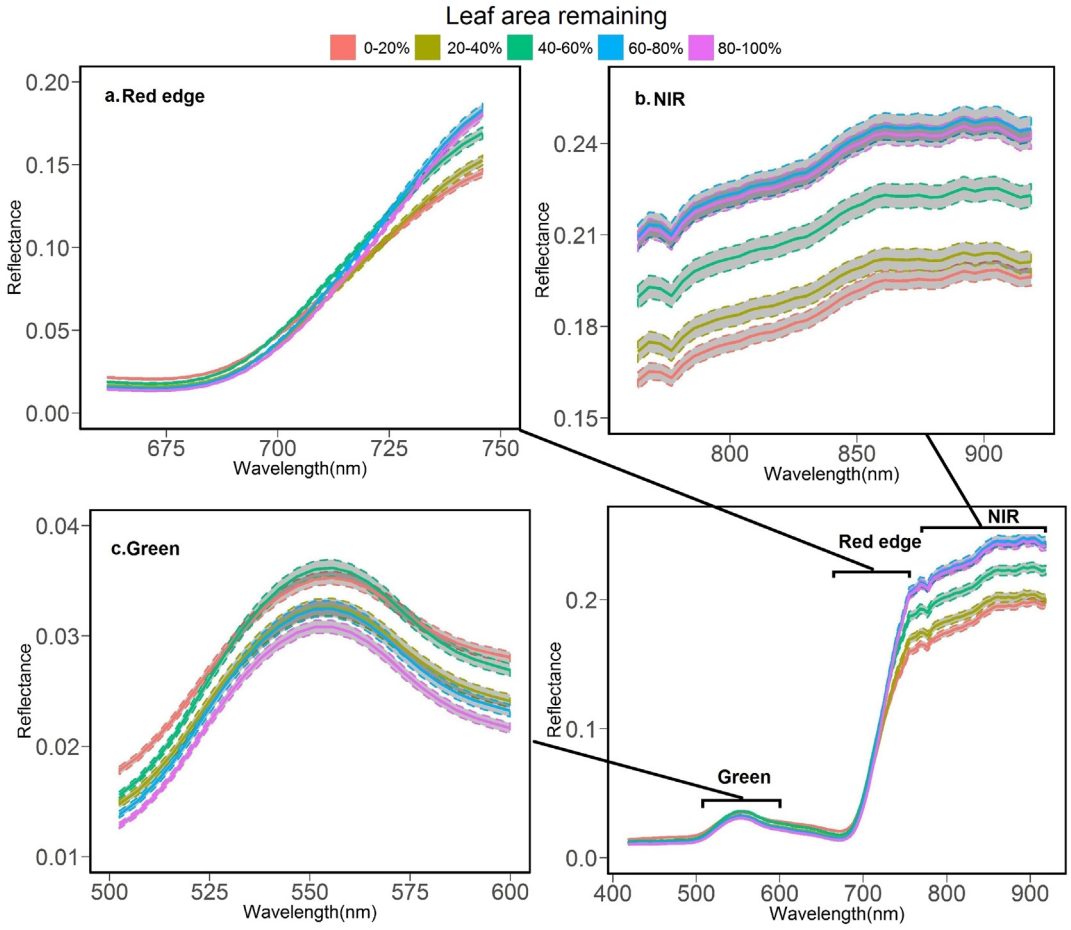

Fig. 4. Mean crown-scale spectra and their 95% confidence interval for the following defoliation severity (i.e., percentage of leaf area remaining) groups extracted from the 2016 G-LiHT imaging spectroscopy measurement: 0–20% leaf area remaining; 20–40% leaf area remaining; 40–60% leaf area remaining; 60–80% leaf area remaining; 80–100% leaf area remaining; To avoid noise, percentage of leaf area remaining was grouped into 20% intervals, consistent with previous similar remote sensing studies (Townsend et al., 2012). (For interpretation of the references to color in this figure legend, the reader is referred to the web version of this article.)

4. Results

4.1. Crown-scale spectral signatures of oak defoliation

To avoid noise and show the general trend of oak spectra across a defoliation severity gradient, surveyed oak crowns were grouped into five defoliation severity levels by an equal 20% interval, and the mean spectra of each severity group were calculated and plotted in Fig. 4, consistent with previous similar remote sensing studies (Townsend et al., 2012). In general, the crown-scale oak spectra were sensitive to defoliation severity, with large spectra variations at green, red edge, and NIR wavelengths (Fig. 4). Specifically, red edge slope, associated with vegetative vigor, decreased with defoliation severity; similarly, NIR reflectance, associated with vegetation biomass, also decreased with defoliation severity. Visible reflectance (e.g., green wavelength) did not demonstrate a clear trend with severity.

4.2. Crown-scale structural changes by oak defoliation

LiDAR-measured canopy height profiles within the five defoliation severity groups varied from 2015 to 2016 (Fig. 6). Most of the defoliation severity groups had positive values at lower vertical height intervals (< 10 m), indicating better penetration of laser pulses through the forest canopy in 2016 and returns from near the surface due to canopy leaf loss. Within the 10–20 m vertical height interval, return points decreased from 2015 to 2016. However, there is no clear trend within the 20–35 m vertical height interval.

4.3. Comparisons of OLS models using IS-only, LiDAR-only and IS + LiDAR variables

We plotted and compared the scatterplots of percentage of leaf area remaining versus 2016 IS and LiDAR metrics for variables with an absolute value of $r \geq 0.40$ (Fig. 6). Among the 3 MESMA fraction and 31 LiDAR metrics, we selected all the MESMA and 11 of the LiDAR-derived predictors (Fig. 6). Specifically, all MESMA related predictors had an absolute value of $r \geq 0.40$ with the percentage of leaf area remaining and were selected for further analysis; in terms of LiDAR-derived structural predictors, nearly all percentile height related predictors except B10 had relatively high linear correlations with crown-scale defoliation severity and demonstrated an increasing trend in correlation with percentile height (Fig. 6). We further calculated the changes from 2015 to 2016 for these predictors with an absolute value of $r \geq 0.40$.

Based on the AIC metric, the most frequently selected important predictor variables differed among the IS-only, LiDAR-only and IS + LiDAR datasets (Table 2). Only the predictors selected > 60 times were used for modeling canopy defoliation for each modeling option (i.e., IS-only, LiDAR-only, and IS + LiDAR; Table 2). Specifically, change in NPV fraction, oak fraction value in 2016, change in understory, and NPV fraction in 2016 were used for IS-only model; B70 in 2016, change in Kurtosis, and intensity skewness in 2016 were used for the LiDAR-only model; for the IS + LiDAR model, B70 in 2016, oak fraction value in 2016, and change in intensity skewness were used. We also calculated the 95% confidence interval of coefficient values of chosen predictors for each dataset option (Table 2).

Validation results varied among the three predictor options (Fig. 7). Overall, the IS-only model had the lowest mapping accuracy with a mean Adj. R value of 0.63, significantly lower ($P < 0.001$) than LiDAR-only and IS + LiDAR models. The validation accuracy of the IS + LiDAR model was only slightly higher than that of LiDAR model (0.81 vs. 0.77), but still statistically significant at the level of 0.05. Using RMSE as a metric, the IS + LiDAR model consistently performed best for mapping canopy defoliation (14.46 ± 2.22%), comparing with the IS-only model (19.11 ± 2.90%) and the LiDAR-only model (15.37 ± 2.12%). Moreover, the value ranges of Adj.R-squared and RMSE (%) for LiDAR-only and IS + LiDAR model were both much less (i.e. 50% and 30%, respectively) than that for IS-only model, signifying much lower modeling uncertainty (Fig. S1). Finally, we found regression coefficients from the different dataset splitting schemes were consistent, in terms of their general pattern and relative magnitude (Table 2).

4.4. Biophysical effects of canopy defoliation

To explore the biophysical effects underpinning the spectral and structural signatures of oak defoliation, we summarized the MESMA fraction values and LiDAR metrics in 2015 and 2016 within the five defoliation severity groups (Figs. 8 and 9). Oak fractional cover generally decreased from 2015 to 2016, but understory and NPV fractional cover indicated the opposite trend (Fig. 8). Specifically, IS measurement captured the increased exposure of forest understory (i.e., shrubs) and NPV materials (i.e., trunk and branch), as a result of decrease in canopy leaf area. More importantly, these changes varied with the defoliation severity, with the largest changes found in highest severity groups (0–20% leaf area remaining). Thus, we conclude that the detected crown-scale spectral and structural signatures in Sections 4.1 & 4.2 can be explained by biophysical effects of insect herbivory including decrease in canopy leaf area and increased exposure in NPV and understory. For LiDAR metrics, B70 (70th bincentile height, Table 1), intensity skewness, and kurtosis all increased from 2015 to 2016, but their change magnitudes decreased with defoliation severity (Fig. 9). These trends are consistent with changes in the canopy height profile within five defoliation severity groups (Fig. 5).

4.5. Crown-scale canopy defoliation across the study area

The final used IS + LiDAR model for mapping crown-scale oak defoliation across the study area was as below.

$$C_d\,(\%) = 100.53 + 36.28 \times M_{oak,2016} - 1.12 \times B70_{2016} + 20.82 \times Skewness_c \quad (2)$$

where C_d stands for percentage of leaf area remaining, $M_{oak,2016}$ for MESMA oak fraction in 2016, $B70_{2016}$ for B70 in 2016, and $Skewness_c$ for change in intensity skewness from 2015 to 2016. It was possible for our model to produce percentage of leaf area remaining < 0% or > 100%. In these cases, we reset the modeled value to the closest physically possible value (0% or 100%). We also split the continuous measurements of percentage of leaf area remaining by the IS + LiDAR model into five groups for map display.

We applied Eq. (2) to the G-LiHT IS + LiDAR dataset covering our study area to map the spatial patterns of canopy leaf status associated with gypsy moth outbreak in 2016 (Fig. 10). Defoliation was scattered in the 2016 map, with large patches of heavy defoliation (0–20% leaf area remaining or 80–100% canopy leaf loss). 2.0% of crown objects suffered heavy defoliation, which is equivalent to 104,811 m^2 of canopy area in our study area. The MEMSA oak fraction, ranging between 0 and 1, and LiDAR B70, ranging between 0 and 100%, corresponded well with the spatial pattern of modeled canopy defoliation status (percentage of leaf area remaining) in our study areas.

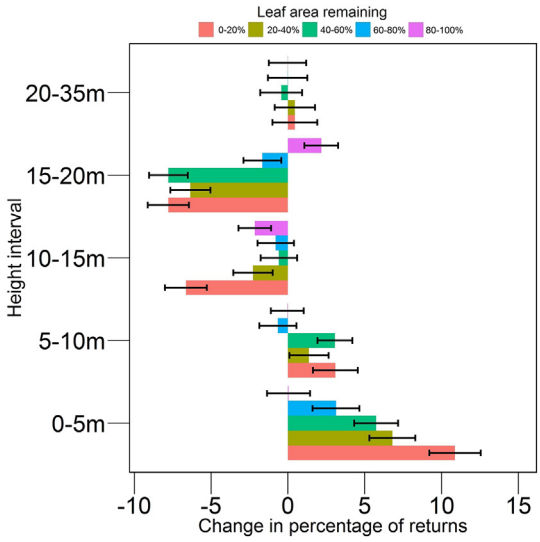

Fig. 5. Change in canopy height profile within five defoliation severity (i.e., percentage of leaf area remaining) groups from 2015 to 2016 calculated from the G-LiHT LiDAR measurements; negative values indicate the decrease in vertical laser return point distributions from 2015 to 2016 at certain height interval, and positive values indicate the opposite trend; bars show the standard errors for each defoliation severity group. To avoid noise, percentage of leaf area remaining was grouped into 20% intervals, consistent with previous similar remote sensing studies (Townsend et al., 2012).

5. Discussion

High resolution canopy defoliation mapping is critical for monitoring and exploring the effects of insect infestations on forest health and ecosystem dynamics, particularly under drier and warmer climate scenarios that may weaken tree defenses to insect attack (Hicke et al., 2012; Seidl et al., 2014; Seidl et al., 2017). We leveraged co-aligned VHR airborne optical IS and structural LiDAR measurements to map defoliation by gypsy moth caterpillars at the individual tree level. We found crown-scale oak spectra at red-edge and NIR wavelengths were most sensitive to defoliation severity, and simple LiDAR metrics (e.g., B70, intensity skewness, and Kurtosis) can effectively detect the crown-scale overall structural changes caused by herbivorous insects. Biophysical effects of canopy leaf loss, particularly exposed understory and NPV, underpinned the detected spectral and structural changes across the defoliation severity gradient. Lastly, we found an IS + LiDAR OLS model had the best mapping performance (Fig. 9) among three predictor options (IS-only, LiDAR-only, and IS + LiDAR), with LiDAR-only outperforming IS-only. We didn't account for spatial effects for the OLS modeling of canopy defoliation in our study, because spatial modeling techniques, such as autoregressive model and spatial filtering (McCarley et al., 2017; Meng et al., 2015), might further improve the accuracy of OLS training models, but would increase the uncertainty of applying the trained model to the whole study area.

Our analysis is distinguished from the previous studies in that we explored the combined hyperspectral and LiDAR-derived structural signatures of deciduous broadleaved trees across a defoliation severity gradient at the individual tree level. Most previous efforts have focused on analyzing spectral signatures of defoliation severity or mortality at ≥30 m plot (i.e., inter-stand) scale with broadband multi-spectral sensors (Radeloff et al., 1999; Rullan-Silva et al., 2013; Senf et al., 2015; Senf et al., 2017c; Townsend et al., 2012), but previous studies also indicate that the pattern of insect outbreak is driven by multi-scale processes (Seidl et al., 2016; Senf et al., 2017a). Thus this study has filled in an important knowledge gap in crown-scale spectral and structural signatures of defoliation severity and provides the groundwork for consistently mapping defoliation severity across multiple

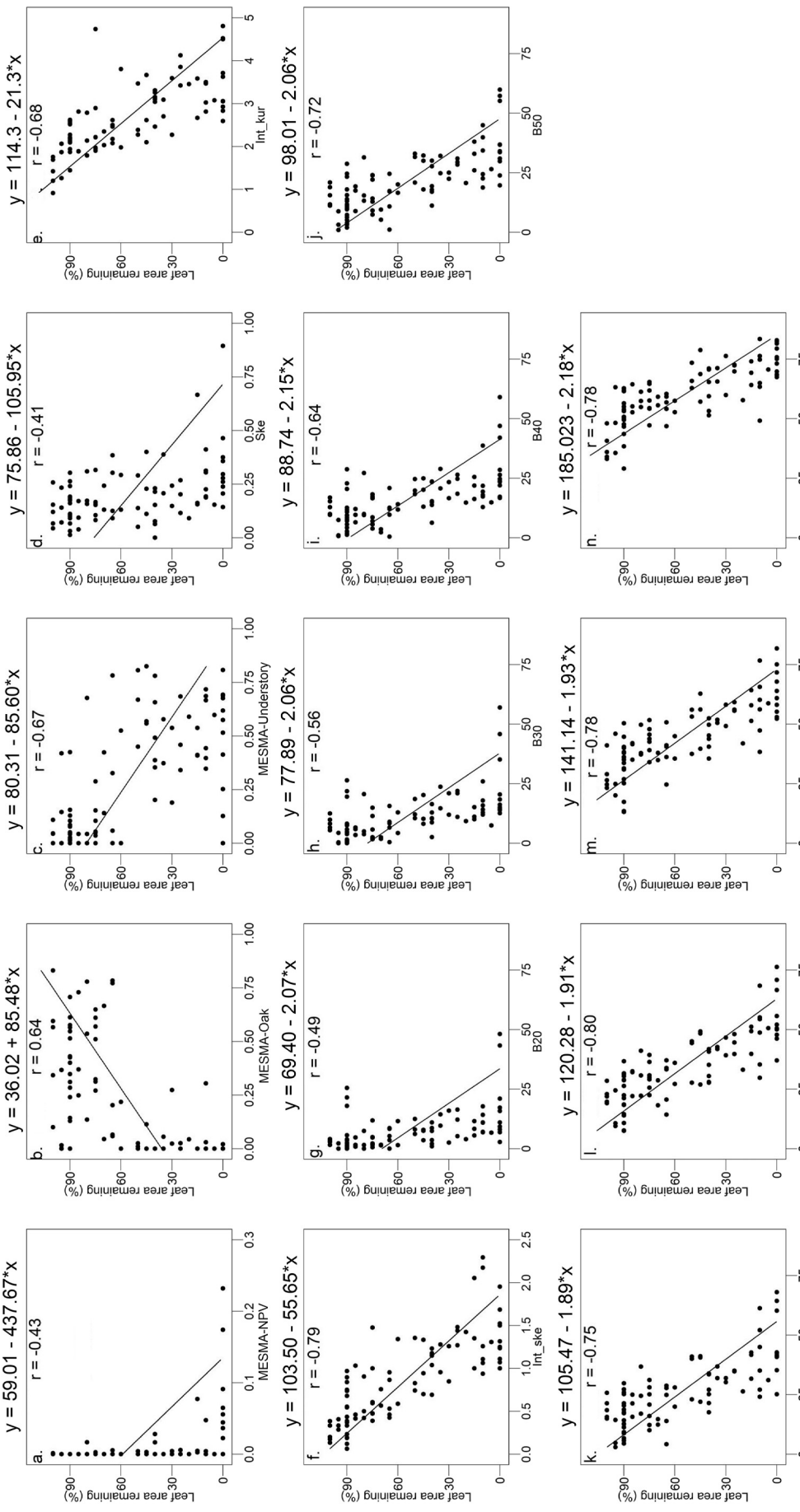

Fig. 6. Scatter plot matrix of percentage of leaf area remaining vs. 2016 IS and LiDAR metrics used for model training: a. MESMA NPV fraction; b. MESMA oak fraction; c. MESMA understory fraction; d. LiDAR skewness; e. LiDAR Intensity kurtosis; f. LiDAR Intensity skewness; g. 20th bincentile height; h. 30th bincentile height; i. 40th bincentile height; j. 50th bincentile height; k. 60th bincentile height; l. 70th bincentile height; m.80th bincentile height; n. 90th bincentile height.

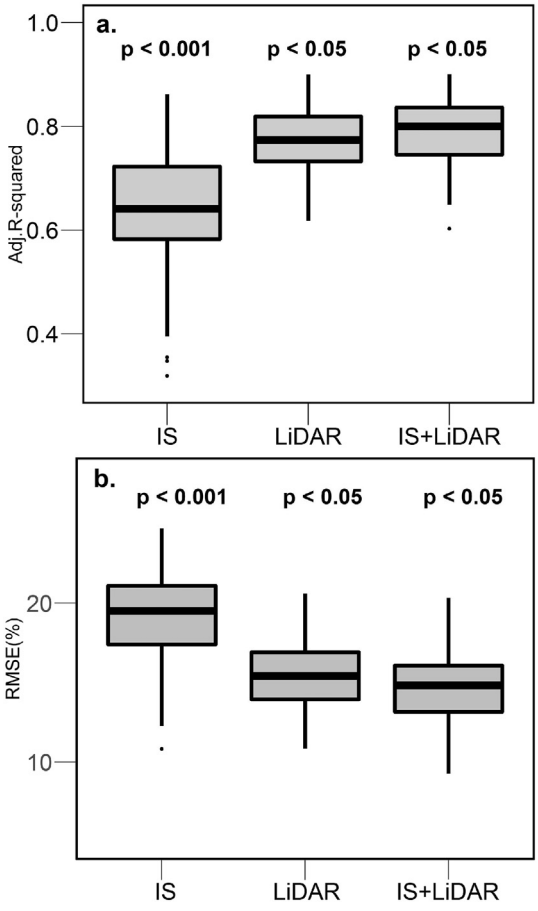

Fig. 7. Boxplots of adjusted R-squared (a) and RMSE (b) values using IS-only predictor variables, LiDAR-only predictor variables and their combination for predicting canopy defoliation of validation datasets. *P* values show the least significance of paired Wilcoxon signed rank test results.

scales, which are critical for forest management and ecological study, as well as for informing and testing of carbon cycle models (Clark et al., 2010; Landry et al., 2016; McDowell et al., 2015; Seidl et al., 2016; Senf et al., 2017a). Specifically, our study indicates that the combined use of VHR IS and LiDAR measurements can provide an opportunity to scale remotely sensed measurements of defoliation severity from the individual-tree level to inter-stand level: on one hand, further studies can be conducted to determine to what extent crown-scale canopy defoliation contributed to the inter-stand scale change in spectral reflectance of broadband multi-spectral sensors like Landsat-8 and Sentinel-2 with higher temporal resolution and larger spatial coverage (Senf et al., 2015; Townsend et al., 2012; Zarco-Tejada et al., 2018); on the other hand, our results can be used to separate the signature of canopy defoliation from other temporal changes (e.g., phenology) that may be present in Landsat or Sentinel-2 data (Hawryło et al., 2018; Senf et al., 2017b). The improved capabilities of remote sensing of insect outbreak at crown-scale can provide new insights for reducing insect habitat quantity and quality and understanding insect outbreak's mechanic process (McDowell et al., 2015; Senf et al., 2017a).

Our study found a negative relationship between NIR reflectance and defoliation severity (Fig. 2), and this relationship is consistent with relationships found by previous studies investigating defoliation of conifers and spruce at inter-stand scale with broadband multi-spectral sensors (Ahern, 1988; Olsson et al., 2012), but different from an increase in NIR reflectance following insect outbreak in jack pine (Radeloff et al., 1999). Our VHR results further indicate that NPV and the forest understory, which were not considered in previous studies, can also affect remotely sensed measurements of oak defoliation and should be taken into account for canopy defoliation mapping, in addition to canopy leaf area (Figs. 6 & 8). The differences in forest understory and structure in varied forest ecosystems can likely explain differences in spectral changes after the insect outbreak across previous studies (Ahern, 1988; Griffiths et al., 2014; Olsson et al., 2012; Radeloff et al., 1999) and the defoliation severity model (Eq. (2)) developed here would have to be adapted for forests with different forest structure, composition and understories. Moreover, our analysis was based on 91 oak crowns in a local forest and segmentation parameters for crown delineations used here (see Section 3.1) can also change with forest type, which further adds to uncertainties in the generalized use of our derived defoliation severity model (Eq. (2)). We thus recommend more spectral and structural signature studies of canopy defoliation across severity gradients at VHR in other forest ecosystems for studying scaling effects and consistent modeling of canopy defoliation across large spatial-temporal scales.

Most previous remote sensing studies of canopy defoliation have focused on the spectral index-based methods (Rullan-Silva et al., 2013; Senf et al., 2017c), which are simple and easy to implement. We have tested the suitability of available visible-NIR narrowband spectral indices in G-LiHT IS data for mapping defoliation severity (Table S2). This analysis demonstrated that red edge indices, such as Modified Red Edge Normalized Difference Vegetation Index (MENDVI) and Vogelmann Red Edge Index 1 (VREI1), had the highest correlations with canopy defoliation caused by insect outbreak (Table S2), which is consistent with previous similar studies (Hawryło et al., 2018; Knipling, 1970; Oumar and Mutanga, 2014; Rock et al., 1988; Shendryk et al., 2016; Townsend et al., 2012). Similar results were also reported in Shendryk et al. (2016), where IS-derived red-edge and NIR variables were the most important ones in predicting tree dieback and defoliation caused by flooding. With the increasing availability of red edge and even shortwave infrared (SWIR) bands on spaceborne remote sensing platforms (i.e., VHR Worldview-3 and moderate-resolution Sentinel-2)

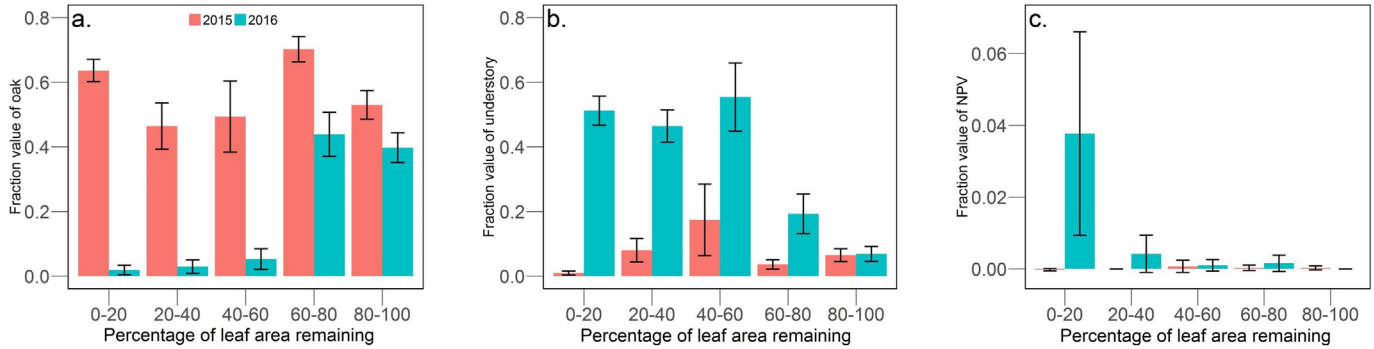

Fig. 8. Average and standard error values of MESMA fractions at five leaf area remaining (i.e., canopy defoliation severity) groups for 2015 and 2016: a. GV-oak fraction; b. GV-understory fraction; c. NPV fraction.

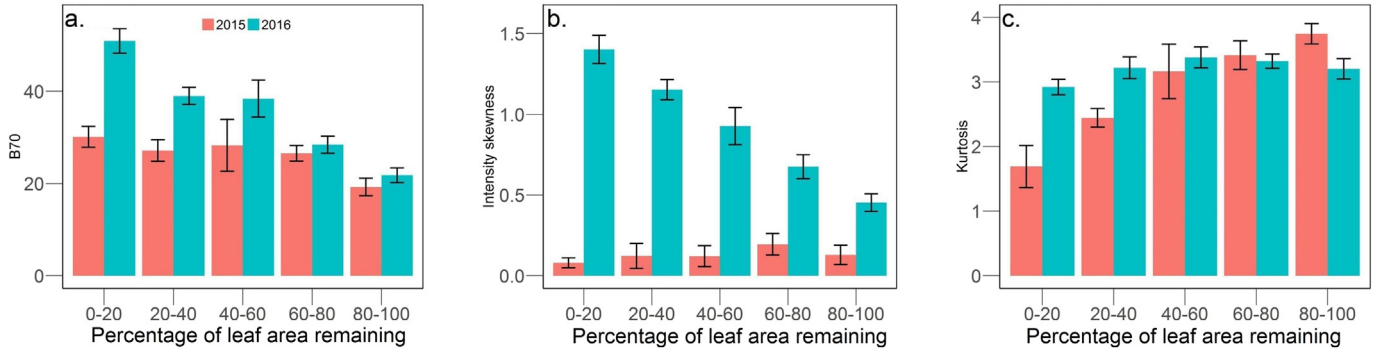

Fig. 9. Average and standard error values of LiDAR predictors selected by stepwise AIC-based method (see Section 4.4) for mapping crown-scale canopy defoliation at five leaf area remaining (i.e., canopy defoliation severity) groups for 2015 and 2016: a. B70; b. Intensity skewness; c. Kurtosis.

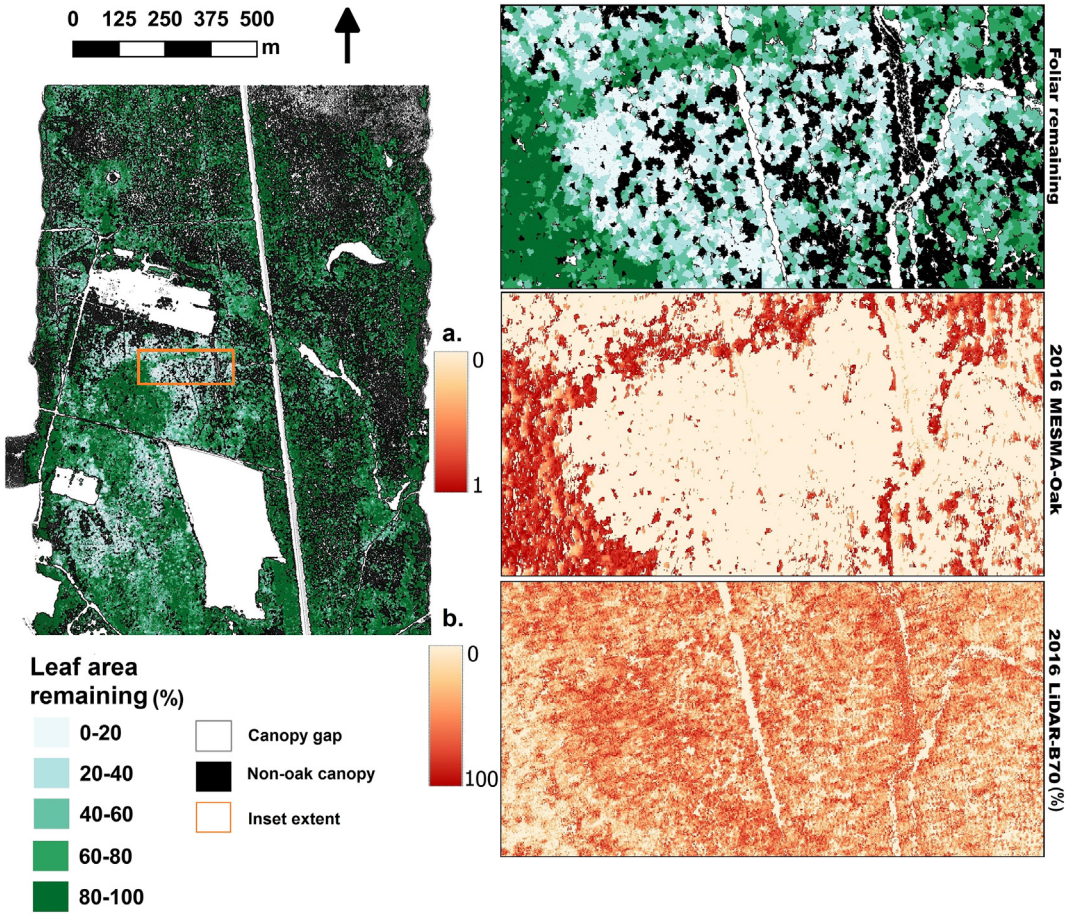

Fig. 10. Crown-scale percentage of oak leaf area remaining (i.e., oak canopy defoliation severity) map at 1 m resolution in a mixed pine-oak forest, Long island, NY in 2016; the inset subplots show a partial zoom-in view of the defoliation severity map and corresponding MESMA oak fraction (a) and LiDAR-derived B70 (i.e., 70th bincentile height) (b). The rectangle on the oak canopy defoliation severity map shows the inset extent.

(Drusch et al., 2012; Warner et al., 2017), more accurate mapping of spatial variation in defoliation severity is promising with these new sensors. Additionally, given the apparent advantages of narrowband vegetation indices and potential for full spectrum metrics like fractional cover, future spaceborne IS mission sensors (e.g., HyspIRI and EnMap) could further improve our capability for mapping insect defoliation despite coarser spatial resolution (Lee et al., 2015; Stuffler et al., 2007). In summary, these mentioned new sensors could potentially enable improved monitoring of the spread and severity of forest infestations across scales, forest types, and disturbance agents with higher accuracy and frequency than ever before. But the G-LiHT IS used here does not cover the SWIR wavelengths, which are sensitive to leaf water content and lignocellulose absorption and have been widely used for remote sensing of canopy defoliation (Somers et al., 2010; Townsend et al., 2012). Metrics using SWIR bands made available by these recent and the planned sensors at moderate spatial resolution thus still require further study to compare their predictive power with LiDAR-derived metrics chosen in this study (Fig. 9). However, previous studies also indicate that visible-NIR wavelengths are still viable for mapping canopy defoliation, in absence of SWIR wavelengths (Townsend et al., 2012).

To examine whether LiDAR can be used for measuring defoliation severity of broadleaf deciduous trees, we explored the sensitivity of various LiDAR metrics to the change in overall canopy structure caused

by herbivorous insects. Previous studies have explored remote sensing of fire-induced structural changes or beetle-induced conifer leaf loss using LiDAR (Alonzo et al., 2017; Hanssen and Solberg, 2007; McCarley et al., 2017; Solberg et al., 2006), but few studies examined the capability of LiDAR metrics for measuring insect-induced broadleaf deciduous tree defoliation severity at the individual tree level. Our analysis shows that simple LiDAR metrics, such as B70 (i.e., 70th bincentile height), intensity skewness and kurtosis, are sensitive to canopy leaf loss by herbivorous insects across the defoliation severity gradient (Fig. 9). This can be explained by the fact that canopy leaf loss by herbivorous insects can increase the chance of LiDAR pulses to penetrate the tree canopies and rebound from the understory, leading to somewhat large variations in vertical profiles of return points, which can increase the LiDAR intensity skewness and kurtosis (Figs. 5 & 9). Additionally, defoliation should provide a distinctive structural signature when compared to fire or logging disturbance (Bolton et al., 2017; Bolton et al., 2015; Kane et al., 2014; Zhao et al., 2015), since insect herbivory doesn't affect branch, trunk, and understory returns. LiDAR data thus may be uniquely capable of mapping different disturbance types based on their structural fingerprint. With the future global LiDAR coverage provided by the Global Ecosystem Dynamics Investigation (GEDI) mission (Dubayah et al., 2014), there is potential to scale up crown-scale measurements of defoliation provided by airborne LiDAR data.

Using airborne IS and LiDAR imaging, our study provides a rapid and accurate approach for regional defoliation severity mapping at the individual tree level. Our validation results of three predictor options (Fig. 9 and Fig. S1) indicate that the combination of IS and LiDAR provide more additional information for mapping defoliation by herbivorous insects than using either sensor type alone, and the LiDAR-only OLS model outperformed the IS-only model, demonstrating that if only one data type could be collected, LiDAR would provide the better ability to map canopy defoliation severity of broadleaf trees. As the development of unmanned remote sensing techniques and computer vision (e.g., Structure from Motion algorithm for three dimensional information construction from two-dimensional image sequences) continues (Alonzo et al., 2018; Colomina and Molina, 2014), the cost of aerial surveys can be further reduced and more studies can be potentially conducted in multiple representative forest ecosystems to scale crown-level defoliation measurements to the inter-stand level, enabling real-time monitoring of canopy defoliation at regional and global scales (Dash et al., 2017; Pasquarella et al., 2017). Considering forest damage caused by herbivorous insects is a function of both the severity and timing of defoliation, more frequent and more accurate spatial-temporal measurements of canopy defoliation are critical to better assisting forest managers with designing adaptive management strategies for reducing forest damage and maintaining forest health. Additionally, the derived high resolution spatial-temporal information would be also essential for exploring insect herbivory effects on ecosystem functioning, diversity, and carbon dynamics (de la Mata et al., 2017; Frost and Hunter, 2004; Goetz et al., 2012; Kenis et al., 2009; Townsend et al., 2004).

6. Conclusion

We explored the crown-level spectral and structural signatures of canopy defoliation by herbivorous insects, as well as underlying biophysical effects, across a defoliation severity gradient using bi-temporal airborne IS and LiDAR measurements. Our results showed that: (1) red edge and NIR spectra are most sensitive to crown-level defoliation severity; (2) LiDAR metrics including B70, intensity skewness, and intensity kurtosis can effectively detect overall canopy structural changes by herbivorous insects and thus can be used for mapping canopy defoliation; (3) In addition to canopy leaf loss, crown-scale biophysical effects of insect herbivory also included increased exposure of understory (e.g., shrub) and NPV (e.g., branch and trunk), which can affect the overall spectral and structural signatures; (4) the IS + LiDAR OLS model (Adj. R-squared = 0.81, RMSE = 14.46%) performed better for measuring canopy defoliation severity than the IS-only (Adj. R-squared = 0.63, RMSE = 19.11%) or LiDAR-only OLS models (Adj. R-squared = 0.77, RMSE = 15.37%). Our aerial survey-based approach, in combination with the current and next generation of spaceborne sensors (e.g., Landsat-8, HyspIRI, EnMap, GEDI, WorldView-3, Sentinel-2), can provide critical information on canopy defoliation over large spatial-temporal scales and thus improve our understanding of the ecological and economic consequences of forest infestations (e.g., reduced growth and increased mortality), as well as implications for forest carbon dynamics. This study serves as one of first efforts for understanding VHR spectral and structural signatures of gypsy moth-caused defoliation in a mixed oak-pine forest, and future work should focus on extending our proposed framework to other types of forests and defoliators/pests.

Acknowledgement

This work was supported by the United States Department of Energy contract No. DE-SC0012704 to Brookhaven National Laboratory. We also thank Dr. Jin Wu and Kathy Schwager for helpful discussions that improved this manuscript.

Appendix A. Supplementary data

Supplementary data to this article can be found online at https://doi.org/10.1016/j.rse.2018.06.008.

References

Ahern, F.J., 1988. The effects of bark beetle stress on the foliar spectral reflectance of lodgepole pine. Int. J. Remote Sens. 9, 1451–1468.
Alonzo, M., Morton, D.C., Cook, B.D., Andersen, H.-E., Babcock, C., Pattison, R., 2017. Patterns of Canopy and Surface Layer Consumption in a Boreal Forest Fire from Repeat Airborne Lidar.
Alonzo, M., Andersen, H.-E., Morton, D.C., Cook, B.D., 2018. Quantifying boreal forest structure and composition using UAV structure from motion. Forests 9, 119.
Asner, G.P., Martin, R.E., Knapp, D.E., Tupayachi, R., Anderson, C.B., Sinca, F., Vaughn, N.R., Llactayo, W., 2017. Airborne laser-guided imaging spectroscopy to map forest trait diversity and guide conservation. Science 355, 385–388.
Ayres, M.P., Lombardero, M.a.J., 2000. Assessing the consequences of global change for forest disturbance from herbivores and pathogens. Sci. Total Environ. 262, 263–286.
Black, S.H., 2005. Logging to Control Insects: The Science and Myths Behind Managing Forest Insect Pests. A Synthesis of Independently Reviewed Research. The Xerces Society for Invertebrate Conservation, Portland.
Bolton, D.K., Coops, N.C., Wulder, M.A., 2015. Characterizing residual structure and forest recovery following high-severity fire in the western boreal of Canada using Landsat time-series and airborne lidar data. Remote Sens. Environ. 163, 48–60.
Bolton, D.K., Coops, N.C., Hermosilla, T., Wulder, M.A., White, J.C., 2017. Assessing variability in post-fire forest structure along gradients of productivity in the Canadian boreal using multi-source remote sensing. J. Biogeogr. 44 (6), 1294–1305.
Burnham, K.P., Anderson, D.R., 2004. Multimodel inference: understanding AIC and BIC in model selection. Sociol. Methods Res. 33, 261–304.
Clark, K.L., Skowronski, N., Hom, J., 2010. Invasive insects impact forest carbon dynamics. Glob. Chang. Biol. 16, 88–101.
Colomina, I., Molina, P., 2014. Unmanned aerial systems for photogrammetry and remote sensing: a review. ISPRS J. Photogramm. Remote Sens. 92, 79–97.
Cook, B.D., Nelson, R.F., Middleton, E.M., Morton, D.C., McCorkel, J.T., Masek, J.G., Ranson, K.J., Ly, V., Montesano, P.M., 2013. NASA Goddard's lidar, hyperspectral and thermal (G-LiHT) airborne imager. Remote Sens. 5, 4045–4066.
Coulson, R.N., McFadden, B.A., Pulley, P.E., Lovelady, C.N., Fitzgerald, J.W., Jack, S.B., 1999. Heterogeneity of forest landscapes and the distribution and abundance of the southern pine beetle. For. Ecol. Manag. 114, 471–485.
Coyle, D.R., Hart, E.R., McMillin, J.D., Rule, L.C., Hall, R.B., 2008. Effects of repeated cottonwood leaf beetle defoliation on Populus growth and economic value over an 8-year harvest rotation. For. Ecol. Manag. 255, 3365–3373.
Dale, V.H., Joyce, L.A., McNulty, S., Neilson, R.P., Ayres, M.P., Flannigan, M.D., Hanson, P.J., Irland, L.C., Lugo, A.E., Peterson, C.J., Simberloff, D., Swanson, F.J., Stocks, B.J., Wotton, B.M., 2001. Climate change and forest disturbances. Bioscience 51, 723–734.
Dash, J.P., Watt, M.S., Pearse, G.D., Heaphy, M., Dungey, H.S., 2017. Assessing very high resolution UAV imagery for monitoring forest health during a simulated disease outbreak. ISPRS J. Photogramm. Remote Sens. 131, 1–14.
De Beurs, K.M., Townsend, P.A., 2008. Estimating the effect of gypsy moth defoliation using MODIS. Remote Sens. Environ. 112, 3983–3990.
de la Mata, R., Hood, S., Sala, A., 2017. Insect outbreak shifts the direction of selection

from fast to slow growth rates in the long-lived conifer *Pinus ponderosa*. Proc. Natl. Acad. Sci., 201700032. http://www.pnas.org/content/early/2017/06/20/1700032114.short.
Dennison, P.E., Roberts, D.A., 2003. Endmember selection for multiple endmember spectral mixture analysis using endmember average RMSE. Remote Sens. Environ. 87, 123–135.
Dennison, P.E., Nagler, P.L., Hultine, K.R., Glenn, E.P., Ehleringer, J.R., 2009. Remote monitoring of tamarisk defoliation and evapotranspiration following saltcedar leaf beetle attack. Remote Sens. Environ. 113, 1462–1472.
Dennison, P.E., Brunelle, A.R., Carter, V.A., 2010. Assessing canopy mortality during a mountain pine beetle outbreak using GeoEye-1 high spatial resolution satellite data. Remote Sens. Environ. 114, 2431–2435.
Drake, N.A., Mackin, S., Settle, J.J., 1999. Mapping vegetation, soils, and geology in semiarid shrublands using spectral matching and mixture modeling of SWIR AVIRIS imagery. Remote Sens. Environ. 68, 12–25.
Drusch, M., Del Bello, U., Carlier, S., Colin, O., Fernandez, V., Gascon, F., Hoersch, B., Isola, C., Laberinti, P., Martimort, P., 2012. Sentinel-2: ESA's optical high-resolution mission for GMES operational services. Remote Sens. Environ. 120, 25–36.
Dubayah, R., Goetz, S.J., Blair, J.B., Fatoyinbo, T.E., Hansen, M., Healey, S.P., Hofton, M.A., Hurtt, G.C., Kellner, J., Luthcke, S.B., 2014. The Global Ecosystem Dynamics Investigation. (In).
Dudley, T.L., Bean, D.W., 2012. Tamarisk biocontrol, endangered species risk and resolution of conflict through riparian restoration. BioControl 57, 331–347.
Elkinton, J.S., Liebhold, A.M., 1990. Population dynamics of gypsy moth in North America. Annu. Rev. Entomol. 35, 571–596.
Fassnacht, F.E., Latifi, H., Ghosh, A., Joshi, P.K., Koch, B., 2014. Assessing the potential of hyperspectral imagery to map bark beetle-induced tree mortality. Remote Sens. Environ. 140, 533–548.
Foster, J.R., Townsend, P.A., Mladenoff, D.J., 2013. Spatial dynamics of a gypsy moth defoliation outbreak and dependence on habitat characteristics. Landsc. Ecol. 28, 1307–1320.
Franklin, S.E., Fan, H., Guo, X., 2008. Relationship between Landsat TM and SPOT vegetation indices and cumulative spruce budworm defoliation. Int. J. Remote Sens. 29, 1215–1220.
Frost, C.J., Hunter, M.D., 2004. Insect canopy herbivory and frass deposition affect soil nutrient dynamics and export in oak mesocosms. Ecology 85, 3335–3347.
Gandhi, K.J.K., Herms, D.A., 2010. Direct and indirect effects of alien insect herbivores on ecological processes and interactions in forests of eastern North America. Biol. Invasions 12, 389–405.
Ghasemi, A., Zahediasl, S., 2012. Normality tests for statistical analysis: a guide for non-statisticians. Int. J. Endocrinol. Metab. 10, 486.
Goetz, S.J., Bond-Lamberty, B., Law, B.E., Hicke, J.A., Huang, C., Houghton, R.A., McNulty, S., O'Halloran, T., Harmon, M., Meddens, A.J.H., 2012. Observations and assessment of forest carbon dynamics following disturbance in North America. J. Geophys. Res. Biogeosci. 117.
Griffith, D.A., 2009. Spatial autocorrelation. Editors-in-Chief In: Rob, K., Nigel, T. (Eds.), International Encyclopedia of Human Geography. Elsevier, Oxford, pp. 308–316.
Griffiths, P., Kuemmerle, T., Baumann, M., Radeloff, V.C., Abrudan, I.V., Lieskovsky, J., Munteanu, C., Ostapowicz, K., Hostert, P., 2014. Forest disturbances, forest recovery, and changes in forest types across the Carpathian ecoregion from 1985 to 2010 based on Landsat image composites. Remote Sens. Environ. 151, 72–88.
Hanavan, R.P., Pontius, J., Hallett, R., 2015. A 10-year assessment of hemlock decline in the catskill mountain region of new York state using hyperspectral remote sensing techniques. J. Econ. Entomol. 108, 339–349.
Hanssen, K.H., Solberg, S., 2007. Assessment of defoliation during a pine sawfly outbreak: calibration of airborne laser scanning data with hemispherical photography. For. Ecol. Manag. 250, 9–16.
Hawryło, P., Bednarz, B., Wężyk, P., Szostak, M., 2018. Estimating defoliation of Scots pine stands using machine-learning methods and vegetation indices of Sentinel-2. Eur. J. Remote Sens. 51, 194–204.
Hicke, J.A., Allen, C.D., Desai, A.R., Dietze, M.C., Hall, R.J., Hogg, E.H., Kashian, D.M., Moore, D., Raffa, K.F., Sturrock, R.N., Vogelmann, J., 2012. Effects of biotic disturbances on forest carbon cycling in the United States and Canada. Glob. Chang. Biol. 18, 7–34.
Hurley, A., Watts, D., Burke, B., Richards, C., 2004. Identifying gypsy moth defoliation in Ohio using Landsat data. Environ. Eng. Geosci. 10, 321–328.
Ji, W.J., Wang, L., Knutson, A.E., 2017. Detection of the spatiotemporal patterns of beetle-induced tamarisk (Tamarix spp.) defoliation along the Lower Rio Grande using Landsat TM images. Remote Sens. Environ. 193, 76–85.
Kane, V.R., North, M.P., Lutz, J.A., Churchill, D.J., Roberts, S.L., Smith, D.F., Mcgaughey, R.J., Kane, J.T., Brooks, M.L., 2014. Assessing fire effects on forest spatial structure using a fusion of Landsat and airborne LiDAR data in Yosemite National Park. Remote Sens. Environ. 151, 89–101.
Kane, V.R., Cansler, C.A., Povak, N.A., Kane, J.T., McGaughey, R.J., Lutz, J.A., Churchill, D.J., North, M.P., 2015. Mixed severity fire effects within the Rim fire: relative importance of local climate, fire weather, topography, and forest structure. For. Ecol. Manag. 358, 62–79.
Kantola, T., Vastaranta, M., Yu, X., Lyytikainen-Saarenmaa, P., Holopainen, M., Talvitie, M., Kaasalainen, S., Solberg, S., Hyyppa, J., 2010. Classification of defoliated trees using tree-level airborne laser scanning data combined with aerial images. Remote Sens. 2, 2665–2679.
Kautz, M., Anthoni, P., Meddens, A.J.H., Pugh, T.A.M., Arneth, A., 2017a. Simulating the recent impacts of multiple biotic disturbances on forest carbon cycling across the United States. Glob. Chang. Biol. 24 (5), 2079–2092.
Kautz, M., Meddens, A.J.H., Hall, R.J., Arneth, A., 2017b. Biotic disturbances in Northern Hemisphere forests - a synthesis of recent data, uncertainties and implications for forest monitoring and modelling. Glob. Ecol. Biogeogr. 26, 533–552.
Kegg, J.D., 1971. The impact of gypsy moth: repeated defoliation of oak in New Jersey. J. For. 69, 852–854.
Kenis, M., Auger-Rozenberg, M.-A., Roques, A., Timms, L., Péré, C., Cock, M.J.W., Settele, J., Augustin, S., Lopez-Vaamonde, C., 2009. Ecological effects of invasive alien insects. Biol. Invasions 11, 21–45.
Knipling, E.B., 1970. Physical and physiological basis for the reflectance of visible and near-infrared radiation from vegetation. Remote Sens. Environ. 1, 155–159.
Kolb, T.E., Fettig, C.J., Ayres, M.P., Bentz, B.J., Hicke, J.A., Mathiasen, R., Stewart, J.E., Weed, A.S., 2016. Observed and anticipated impacts of drought on forest insects and diseases in the United States. For. Ecol. Manag. 380, 321–334.
Kurczewski, F.E., Boyle, H.F., 2000. Historical changes in the pine barrens of central Suffolk County, New York. Northeast. Nat. 7, 95–112.
Landry, J.S., Price, D.T., Ramankutty, N., Parrott, L., Matthews, H.D., 2016. Implementation of a Marauding Insect Module (MIM, version 1.0) in the Integrated BIosphere Simulator (IBIS, version 2.6b4) dynamic vegetation–land surface model. Geosci. Model Dev. 9, 1243–1261.
Landsber, J., Ohmart, C., 1989. Levels of insect defoliation in forests: patterns and concepts. Trends Ecol. Evol. 4, 96–100.
Lausch, A., Erasmi, S., King, D.J., Magdon, P., Heurich, M., 2016. Understanding forest health with remote sensing-part I—a review of spectral traits, processes and remote-sensing characteristics. Remote Sens. 8, 1029.
Lee, C.M., Cable, M.L., Hook, S.J., Green, R.O., Ustin, S.L., Mandl, D.J., Middleton, E.M., 2015. An introduction to the NASA Hyperspectral InfraRed Imager (HyspIRI) mission and preparatory activities. Remote Sens. Environ. 167, 6–19.
Lewis, S.A., Hudak, A.T., Robichaud, P.R., Morgan, P., Satterberg, K.L., Strand, E.K., Smith, A.M.S., Zamudio, J.A., Lentile, L.B., 2017. Indicators of burn severity at extended temporal scales: a decade of ecosystem response in mixed-conifer forests of western Montana. Int. J. Wildland Fire 26, 755–771.
Li, W.K., Guo, Q.H., Jakubowski, M.K., Kelly, M., 2012. A new method for segmenting individual trees from the lidar point cloud. Photogramm. Eng. Remote. Sens. 78, 75–84.
Lippitt, C.D., Rogan, J., Toledano, J., Sangermano, F., Eastman, J.R., Mastro, V., Sawyer, A., 2008. Incorporating anthropogenic variables into a species distribution model to map gypsy moth risk. Ecol. Model. 210, 339–350.
Logan, J.A., Régnière, J., Powell, J.A., 2003. Assessing the impacts of global warming on forest pest dynamics. Front. Ecol. Environ. 1, 130–137.
Lu, X., Guo, Q., Li, W., Flanagan, J., 2014. A bottom-up approach to segment individual deciduous trees using leaf-off lidar point cloud data. ISPRS J. Photogramm. Remote Sens. 94, 1–12.
Man, G., 2010. Major Forest Insect and Disease Conditions in the United States: 2009 Update. USDA Forest Service.
McCarley, T.R., Kolden, C.A., Vaillant, N.M., Hudak, A.T., Smith, A.M., Wing, B.M., Kellogg, B.S., Kreitler, J., 2017. Multi-temporal LiDAR and Landsat quantification of fire-induced changes to forest structure. Remote Sens. Environ. 191, 419–432.
McDowell, N.G., Coops, N.C., Beck, P.S.A., Chambers, J.Q., Gangodagamage, C., Hicke, J.A., Huang, C.-y., Kennedy, R., Krofcheck, D.J., Litvak, M., 2015. Global satellite monitoring of climate-induced vegetation disturbances. Trends Plant Sci. 20, 114–123.
Meng, R., Dennison, P.E., 2015. Spectroscopic analysis of green, desiccated and dead tamarisk canopies. Photogramm. Eng. Remote. Sens. 81, 199–207.
Meng, R., Zhao, F., 2017. Remote sensing of fire effects: a review for recent advances in burned area and burn severity mapping. In: Petropoulos, G.P., Islam, T. (Eds.), Remote Sensing of Hydrometeorological Hazards. CRC Press/Taylor & Francis Group, Boca Raton, FL, pp. 261–281.
Meng, R., Dennison, P., Jamison, L., van Riper, C., Nager, P., Hultine, K., Bean, D., Dudley, T., 2012. Detection of tamarisk defoliation by the northern tamarisk beetle based on multitemporal Landsat 5 thematic mapper imagery. GISci. Remote Sens. 49, 510–537.
Meng, R., Dennison, P.E., Huang, C., Moritz, M.A., D'Antonio, C., 2015. Effects of fire severity and post-fire climate on short-term vegetation recovery of mixed-conifer and red fir forests in the Sierra Nevada Mountains of California. Remote Sens. Environ. 171, 311–325.
Meng, R., Wu, J., Schwager, K.L., Zhao, F., Dennison, P.E., Cook, B.D., Brewster, K., Green, T.M., Serbin, S.P., 2017. Using high spatial resolution satellite imagery to map forest burn severity across spatial scales in a Pine Barrens ecosystem. Remote Sens. Environ. 191, 95–109.
Meng, R., Wu, J., Zhao, F., Cook, B.D., Hanavan, R.P., Serbin, S.P., 2018. Measuring short-term post-fire forest recovery across a burn severity gradient in a mixed pine-oak forest using multi-sensor remote sensing techniques. Remote Sens. Environ. 210, 282–296.
Millar, C.I., Stephenson, N.L., 2015. Temperate forest health in an era of emerging megadisturbance. Science 349, 823–826.
Nagler, P.L., Pearlstein, S., Glenn, E.P., Brown, T.B., Bateman, H.L., Bean, D.W., Hultine, K.R., 2014. Rapid dispersal of saltcedar (Tamarix spp.) biocontrol beetles (*Diorhabda carinulata*) on a desert river detected by phenocams, MODIS imagery and ground observations. Remote Sens. Environ. 140, 206–219.
Naidoo, R., Lechowicz, M.J., 2001. Effects of gypsy moth on radial growth of deciduous trees. For. Sci. 47, 338–348.
O'brien, R.M., 2007. A caution regarding rules of thumb for variance inflation factors. Qual. Quant. 41, 673–690.
Olsson, P.-O., Jönsson, A.M., Eklundh, L., 2012. A new invasive insect in Sweden – Physokermes inopinatus: tracing forest damage with satellite based remote sensing. For. Ecol. Manag. 285, 29–37.
Oumar, Z., Mutanga, O., 2014. Integrating environmental variables and WorldView-2 image data to improve the prediction and mapping of *Thaumastocoris peregrinus*

(bronze bug) damage in plantation forests. ISPRS J. Photogramm. Remote Sens. 87, 39–46.
Parkan, M., 2017. Digital forestry toolbox (In). http://mparkan.github.io/Digital-Forestry-Toolbox/.
Pasquarella, V.J., Bradley, B.A., Woodcock, C.E., 2017. Near-real-time monitoring of insect defoliation using Landsat time series. Forests 8, 275.
Quintano, C., Fernández-Manso, A., Roberts, D.A., 2013. Multiple Endmember Spectral Mixture Analysis (MESMA) to map burn severity levels from Landsat images in Mediterranean countries. Remote Sens. Environ. 136, 76–88.
Radeloff, V.C., Mladenoff, D.J., Boyce, M.S., 1999. Detecting Jack pine budworm defoliation using spectral mixture analysis: separating effects from determinants. Remote Sens. Environ. 69, 156–169.
Reiners, W., 1967. Relationships between vegetational strata in the pine barrens of central Long Island, New York. Bull. Torrey. Bot. Club 87–99.
Roberts, D.A., Gardner, M., Church, R., Ustin, S., Scheer, G., Green, R.O., 1998. Mapping chaparral in the Santa Monica Mountains using multiple endmember spectral mixture models. Remote Sens. Environ. 65, 267–279.
Roberts, D., Halligan, K., Dennison, P., 2007. VIPER Tools user manual. UC Santa Barbara, Department of Geography, Visualization and Image Processing for Environmental Research Laboratory.
Rock, B.N., Hoshizaki, T., Miller, J.R., 1988. Comparison of in situ and airborne spectral measurements of the blue shift associated with forest decline. Remote Sens. Environ. 24, 109–127.
Rullan-Silva, C.D., Olthoff, A.E., de la Mata, J.A.D., Pajares-Alonso, J.A., 2013. Remote monitoring of forest insect defoliation-a review. Forest Syst. 22, 377–391.
Seidl, R., Schelhaas, M.-J., Rammer, W., Verkerk, P.J., 2014. Increasing forest disturbances in Europe and their impact on carbon storage. Nat. Clim. Chang. 4, 806–810.
Seidl, R., Müller, J., Hothorn, T., Bässler, C., Heurich, M., Kautz, M., 2016. Small beetle, large-scale drivers: how regional and landscape factors affect outbreaks of the European spruce bark beetle. J. Appl. Ecol. 53, 530–540.
Seidl, R., Thom, D., Kautz, M., Martin-Benito, D., Peltoniemi, M., Vacchiano, G., Wild, J., Ascoli, D., Petr, M., Honkaniemi, J., 2017. Forest disturbances under climate change. Nat. Clim. Chang. 7, 395–402.
Senf, C., Pflugmacher, D., Wulder, M.A., Hostert, P., 2015. Characterizing spectral–temporal patterns of defoliator and bark beetle disturbances using Landsat time series. Remote Sens. Environ. 170, 166–177.
Senf, C., Campbell, E.M., Pflugmacher, D., Wulder, M.A., Hostert, P., 2017a. A multi-scale analysis of western spruce budworm outbreak dynamics. Landsc. Ecol. 32, 501–514.
Senf, C., Pflugmacher, D., Heurich, M., Krueger, T., 2017b. A Bayesian hierarchical model for estimating spatial and temporal variation in vegetation phenology from Landsat time series. Remote Sens. Environ. 194, 155–160.
Senf, C., Seidl, R., Hostert, P., 2017c. Remote sensing of forest insect disturbances: current state and future directions. Int. J. Appl. Earth Obs. Geoinf. 60, 49–60.
Shendryk, I., Broich, M., Tulbure, M.G., McGrath, A., Keith, D., Alexandrov, S.V., 2016. Mapping individual tree health using full-waveform airborne laser scans and imaging spectroscopy: a case study for a floodplain eucalypt forest. Remote Sens. Environ. 187, 202–217.
Solberg, S., Naesset, E., Hanssen, K.H., Christiansen, E., 2006. Mapping defoliation during a severe insect attack on Scots pine using airborne laser scanning. Remote Sens. Environ. 102, 364–376.
Somers, B., Verbesselt, J., Ampe, E.M., Sims, N., Verstraeten, W.W., Coppin, P., 2010. Spectral mixture analysis to monitor defoliation in mixed-aged *Eucalyptus globulus* Labill plantations in southern Australia using Landsat 5-TM and EO-1 Hyperion data. Int. J. Appl. Earth Obs. Geoinf. 12, 270–277.
Spruce, J.P., Sader, S., Ryan, R.E., Smoot, J., Kuper, P., Ross, K., Prados, D., Russell, J., Gasser, G., McKellip, R., Hargrove, W., 2011. Assessment of MODIS NDVI time series data products for detecting forest defoliation by gypsy moth outbreaks. Remote Sens. Environ. 115, 427–437.
Stuffler, T., Kaufmann, C., Hofer, S., Förster, K.P., Schreier, G., Müller, A., Eckardt, A., Bach, H., Penne, B., Benz, U., 2007. The EnMAP hyperspectral imager—an advanced optical payload for future applications in Earth observation programmes. Acta Astronaut. 61, 115–120.
Thompson, L.M., Faske, T.M., Banahene, N., Grim, D., Agosta, S.J., Parry, D., Tobin, P.C., Johnson, D.M., Grayson, K.L., 2017. Variation in growth and developmental responses to supraoptimal temperatures near latitudinal range limits of gypsy moth *Lymantria dispar* (L.), an expanding invasive species. Physiol. Entomol. 42, 181–190.
Townsend, P.A., Eshleman, K.N., Welcker, C., 2004. Remote sensing of gypsy moth defoliation to assess variations in stream nitrogen concentrations. Ecol. Appl. 14, 504–516.
Townsend, P.A., Singh, A., Foster, J.R., Rehberg, N.J., Kingdon, C.C., Eshleman, K.N., Seagle, S.W., 2012. A general Landsat model to predict canopy defoliation in broadleaf deciduous forests. Remote Sens. Environ. 119, 255–265.
Trumbore, S., Brando, P., Hartmann, H., 2015. Forest health and global change. Science 349, 814–818.
Warner, T.A., Skowronski, N.S., Gallagher, M.R., 2017. High spatial resolution burn severity mapping of the New Jersey Pine Barrens with WorldView-3 near-infrared and shortwave infrared imagery. Int. J. Remote Sens. 38, 598–616.
White, J.C., Wulder, M.A., Brooks, D., Reich, R., Wheate, R.D., 2005. Detection of red attack stage mountain pine beetle infestation with high spatial resolution satellite imagery. Remote Sens. Environ. 96, 340–351.
White, J.C., Coops, N.C., Wulder, M.A., Vastaranta, M., Hilker, T., Tompalski, P., 2016. Remote sensing technologies for enhancing forest inventories: a review. Can. J. Remote. Sens. 42, 619–641.
Wulder, M.A., White, J.C., Coops, N.C., Butson, C.R., 2008. Multi-temporal analysis of high spatial resolution imagery for disturbance monitoring. Remote Sens. Environ. 112, 2729–2740.
Yamashita, T., Yamashita, K., Kamimura, R., 2007. A stepwise AIC method for variable selection in linear regression. Commun. Stat. Theory Methods 36, 2395–2403.
Zarco-Tejada, P.J., Hornero, A., Hernández-Clemente, R., Beck, P.S.A., 2018. Understanding the temporal dimension of the red-edge spectral region for forest decline detection using high-resolution hyperspectral and Sentinel-2a imagery. ISPRS J. Photogramm. Remote Sens. 137, 134–148.
Zhao, F., Huang, C., Zhu, Z., 2015. Use of vegetation change tracker and support vector machine to map disturbance types in greater yellowstone ecosystems in a 1984–2010 Landsat time series. IEEE Geosci. Remote Sens. Lett. 12, 1650–1654.